

Electronic supporting information: Amorphous-like thermal conductivity and high thermoelectric figure of merit in “ π ” SnS and SnSe

Min Zhang, Ioanna Pallikara, Joseph M. Flitcroft, and Jonathan M. Skelton

1 Computational methods

1.1 Calculation and analysis of lattice thermal conductivity within the single-mode relaxation-time approximation

In this work, the lattice thermal conductivity from “particle-like” transport, κ_p , was computed by solving the phonon Boltzmann transport equation (BTE) within the single-mode relaxation-time approximation (SM-RTA). In the SM-RTA, the κ_p is calculated as:¹

$$\kappa_p = \frac{1}{N_q V} \sum_{qj} \kappa_{qj}(T) = \frac{1}{NV} \sum_{qj} C_{qj}(T) \mathbf{v}_{qj} \otimes \mathbf{v}_{qj} \tau_{qj} \quad (1)$$

where the sum runs over N_q wavevectors \mathbf{q} and $3n_a$ band indices j , V is the unit-cell volume, and the κ_{qj} are the modal contributions to the macroscopic κ determined by the heat capacities C_{qj} , group velocities \mathbf{v}_{qj} and lifetimes τ_{qj} .

To analyse the SM-RTA κ_p , we first separate the κ_p into harmonic and weighted-average lifetime components according to:²⁻⁴

$$\kappa_p = \tau^{\text{CRTA}} \times \frac{1}{N_q V} \sum_{qj} \frac{\kappa_{qj}}{\tau_{qj}} = \tau^{\text{CRTA}} \times \frac{1}{NV} \sum_{qj} C_{qj}(T) \mathbf{v}_{qj} \otimes \mathbf{v}_{qj} \quad (2)$$

Differences in the $\kappa/\tau^{\text{CRTA}}$ reflect differences in the (harmonic) phonon group velocities, while differences in the τ^{CRTA} are indicative of differences in the (anharmonic) phonon lifetimes.

The phonon lifetimes can be further analysed in terms of the “phase spaces” of allowed energy- and momentum-conserving scattering pathways and the three-phonon interaction strengths according to:^{3,4}

$$\tau^{-1} = \frac{36\pi}{\hbar^2} \bar{P} \bar{N}_2(f) \quad (3)$$

$\bar{N}_2(f)$ is a phase-space function, computed from the harmonic phonon spectra, that counts the average number of energy- and momentum conserving three-phonon scattering pathways for a phonon with frequency f_{qj} . The \bar{P} are weighted-average anharmonic three-phonon interaction strengths calculated from the harmonic frequencies and eigenvectors and the third-order force constants.¹ Differences in the $\bar{N}_2(f)$ allow for a qualitative assessment of the impact of the selection rules, determined by the shape of the phonon spectrum, on the phonon lifetimes, while the \bar{P} allow for quantitative comparison of the three-phonon interaction strengths.⁴ We note that, unlike the $\kappa/\tau^{\text{CRTA}}$ and τ^{CRTA} , the $\bar{N}_2(f)$ and \bar{P} are both “extensive” quantities, and must be divided and multiplied, respectively, by the number of bands per wavevector, $(3n_a)^2$, to be compared between systems.

1.2 Calculation of electrical transport properties

The electrical properties were calculated by solving the electron Boltzmann transport equations within the momentum relaxation-time approximation (MRTA) with approximate models for the electron scattering rates.^{5,6} In this approach, the electrical conductivity, Seebeck coefficient and electronic thermal conductivity are obtained from the n^{th} -order moments of the generalised transport coefficients $\mathbf{L}^n(\varepsilon_F, T)$:⁵

$$\boldsymbol{\sigma}(\varepsilon_F, T) = \mathbf{L}^0(\varepsilon_F, T) \quad (4)$$

$$\mathbf{S}(\varepsilon_F, T) = \frac{1}{eT} \frac{\mathbf{L}^1(\varepsilon_F, T)}{\mathbf{L}^0(\varepsilon_F, T)} \quad (5)$$

$$\kappa_{\text{el}}(\varepsilon_F, T) = \frac{1}{e^2 T} \left\{ \frac{[\mathbf{L}^1(\varepsilon_F, T)]^2}{\mathbf{L}^0(\varepsilon_F, T)} - \mathbf{L}^2(\varepsilon_F, T) \right\} \quad (6)$$

where ε_F is the Fermi energy and e is the elementary charge. The \mathbf{L}^n are calculated as:

$$\mathbf{L}^n(\varepsilon_F, T) = e^2 \int \boldsymbol{\Sigma}(\varepsilon, T) (\varepsilon - \varepsilon_F)^n \left[-\frac{\partial f(\varepsilon, \varepsilon_F, T)}{\partial \varepsilon} \right] d\varepsilon \quad (7)$$

where the spectral conductivity $\boldsymbol{\Sigma}$ and Fermi-Dirac function f are given by:

$$\boldsymbol{\Sigma}(\varepsilon, T) = \frac{1}{8\pi^3} \sum_j \int \mathbf{v}_{\mathbf{k}j} \otimes \mathbf{v}_{\mathbf{k}j} \tau_{kj}(T) (\varepsilon - \varepsilon_{kj}) d\mathbf{k} \quad (8)$$

$$f(\varepsilon, \varepsilon_F, T) = \frac{1}{\exp[(\varepsilon - \varepsilon_F)/k_B T] + 1} \quad (9)$$

In Eq. 4-9 the ε_{kj} , \mathbf{v}_{kj} and τ_{kj} are the electron band energies, group velocities and lifetimes, respectively, ε_F is the Fermi energy, which is determined by the density of states and an extrinsic carrier concentration (“doping level”) n , and k_B is the Boltzmann constant.

The electron lifetimes are determined by combining the scattering rates (inverse lifetimes) from approximate models for four scattering processes common to semiconductor materials, *viz.* acoustic deformation potential (ADP), ionized impurity (IMP), piezoelectric

(PIE), and polar optical phonon (POP) scattering:⁶

$$\tau^{-1} = \tau_{\text{ADP}}^{-1} + \tau_{\text{IMP}}^{-1} + \tau_{\text{PIE}}^{-1} + \tau_{\text{POP}}^{-1} \quad (10)$$

The expressions for the rates are somewhat involved, and full details can be found in Ref. ⁶.

1.3 Scalar averaging of tensor quantities

The four properties that determine the thermoelectric figure of merit ZT , viz. the electrical conductivity σ , Seebeck coefficient S and the lattice and electronic thermal conductivity $\kappa_{\text{latt}}/\kappa_{\text{el}}$, are 3×3 tensors. In cubic spacegroups, the three diagonal elements of the tensors \mathbf{T} , corresponding to transport along the Cartesian x , y and z directions, are equivalent and equal to the scalar average given by:

$$T = \frac{1}{3} \text{Tr}[\mathbf{T}] = \frac{1}{3} (T_{xx} + T_{yy} + T_{zz}) \quad (11)$$

We denote the averages T (i.e. in Roman type) to distinguish them from the tensor quantities \mathbf{T} (bold type). (For completeness, the “particle-like” and “wave-like” intraband-tunnelling contributions to the κ_{latt} , $\kappa_{\text{p}}/\kappa_{\text{w}}$ are also tensors and can be averaged in the same way. Except for Fig. 4(b) in the text, where we show the average κ_{latt} and the minimum κ_{yy} along the b axis of $Pnma$ SnS and SnSe, we present and discuss the scalar averages in the text.

1.4 Approximate lattice thermal conductivity of π cubic models with expanded unit-cell volumes

The κ_{latt} of π SnS and SnSe models with expanded unit-cell volumes was estimated using the approximate model developed in previous studies.^{3,7}

Approximate phonon linewidths $\tilde{\Gamma}_{\mathbf{q}j}$ are calculated from:¹

$$\tilde{\Gamma}_{\mathbf{q}j} = \frac{36\pi}{\hbar^2} P_{\mathbf{q}j} N_2(\mathbf{q}, \omega_{\mathbf{q}j}, T) \quad (12)$$

The function N_2 captures the “phase space” of energy- and momentum-conserving scattering channels available to a phonon with frequency $\omega_{\mathbf{q}j}$ and wavevector \mathbf{q} and is given by:

$$\begin{aligned} N_2(\mathbf{q}, \omega, T) = & \frac{1}{N_{\mathbf{q}}} \sum_{\mathbf{q}'j', \mathbf{q}''j''} [\Delta(\mathbf{q}, \mathbf{q}', \mathbf{q}'') \times \{ [n_{\mathbf{q}'j'}(T) - n_{\mathbf{q}''j''}(T)] [\delta(\omega + \omega_{\mathbf{q}'j'} - \omega_{\mathbf{q}''j''}) + \delta(\omega - \omega_{\mathbf{q}'j'} + \omega_{\mathbf{q}''j''})] \\ & + [n_{\mathbf{q}'j'}(T) + n_{\mathbf{q}''j''}(T) + 1] \delta(\omega + \omega_{\mathbf{q}'j'} + \omega_{\mathbf{q}''j''}) \} \end{aligned} \quad (13)$$

where functions δ and Δ enforce conservation of energy and crystal momentum, respectively, and the $n_{\mathbf{q}j}$ are the phonon occupation numbers from the Bose-Einstein distribution:

$$n_{\mathbf{q}j}(T) = \frac{1}{\exp[\hbar\omega_{\mathbf{q}j}/k_{\text{B}}T] - 1} \quad (14)$$

By setting the averaged three-phonon interactions strengths $P_{\mathbf{q}j}$ in Eq. 12 to a weighted-average value \tilde{P} determined at the equilibrium volume V_0 , it is possible to estimate the κ_{latt} of expanded unit cells under the assumption of similar three-phonon interaction strengths to those at $V = V_0$. In principle, the $P_{\mathbf{q}j}$ and \tilde{P} are temperature independent, but in practice the \tilde{P} are weakly T -dependent.² In the present calculations, we use the \tilde{P} determined at $V = V_0$ and $T = 300$ K.

1.5 Calculation of Fermi surface complexity factor

The Fermi surface complexity factor $N_{\text{V}}^* K^*$ is given by:⁸

$$N_{\text{V}}^* K^* = \left(\frac{m_{\text{S}}^*}{m_{\text{C}}^*} \right)^{3/2} \quad (15)$$

where N_{V}^* is the effective valley degeneracy, K^* is the effective anisotropy factor, and m_{S}^* and m_{C}^* are the Seebeck and conductivity effective masses.

Using the constant-relaxation time approximation (CRTA) for the electronic properties, where the electron lifetimes in Eq. 8 are set to a constant value $\tau_{\mathbf{k}j} = \tau^{\text{el}}$, the m_{C}^* are given by:

$$\sigma = ne\mu = \frac{ne^2\tau^{\text{el}}}{m_{\text{C}}^*} \rightarrow m_{\text{C}}^* = \frac{ne^2\tau^{\text{el}}}{\sigma} \quad (16)$$

We note that σ , n , μ and m_{C}^* depend on the Fermi level ε_{F} , and also the temperature T since this may affect the position of the Fermi level. However, the dependence of the m_{C}^* on ε_{F} for a given carrier type is expected to be relatively weak.⁸

To determine the m_s^* , we follow the procedure in Ref. ⁸. We first determine the effective chemical potential η_{eff} that would yield the Seebeck coefficient for a single parabolic band:

$$S(\mu) = \frac{k}{\pm e} \left[\frac{(2+\lambda) F_{1+\lambda}(\eta_{\text{eff}})}{(1+\lambda) F_{\lambda}(\eta_{\text{eff}})} - \eta_{\text{eff}} \right] \quad (17)$$

where the sign of the charge is chosen based on the carrier type (+ve for holes, -v efor electrons), the scattering exponent $\lambda = 1/2$ for the CRTA, and the $f_j(\eta)$ are given by:

$$F_j(\eta) = \int_0^{\infty} \frac{\epsilon^j}{1 + \exp[\epsilon - \eta]} d\epsilon \quad (18)$$

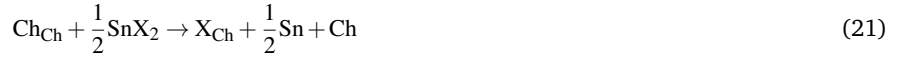
Once η_{eff} has been determined, we then calculate m_s^* according to:

$$n = \frac{1}{2\pi^2} \left[\frac{2m_s^* k_B T}{\hbar^2} \right]^{3/2} F_{1/2}(\eta_{\text{eff}}) \rightarrow m_s^* = \frac{\hbar^2}{2k_B T} \left[\frac{2\pi^2 n}{F_{1/2}(\eta_{\text{eff}})} \right]^{2/3} \quad (19)$$

We again note that the n , η_{eff} and, hence, m_s^* depend on the Fermi level and temperature, but the m_s^* is expected to be relatively constant with respect to the ϵ_F .

1.6 Calculations on doped $Pnma$ and π SnS and $SnSe$

The doping energies E_d for incorporating Na, Ag, Cl, Br, Sb and Bi into the $Pnma$ and π phases of SnS and $SnSe$ were determined from the forward energies of the following reactions:



where M is a metal substituting at an Sn site and X is a halogen substituting at a chalcogen (Ch) site. These processes were chosen based on the fact that metal-doped tin chalcogenides are typically formed from the elemental solids,^{7,9-11} whereas halogen-doped chalcogenies are usually formed from elemental Sn, S/Se and the tin dihalide SnX_2 .¹²⁻¹⁴

The degree of ionisation of the dopant was determined by analysing the electronic density of states $g(E)$ (DoS). Noting that none of the dopants we tested form defect levels, we first located the centre of the $SnCh$ bandgap in the DoS from a plateau in the integrated $g(E)$ (IDoS) at the relative number of valence electrons corresponding to the undoped host. We then calculated the difference in the IDoS between the centre of the gap and the calculated Fermi energy E_F .

Precipitation energies E_p for exsolution of the pure metal chalcogenide phases from metal-doped $SnCh$ in the presence of a chalcogen reservoir were determined from the forward energies of the following reaction:



Exsolution of Na/Ag as M_2S is accompanied by 0.5 equivalents of the chalcogen, whereas exsolution of Bi/Ag as M_2S_3 requires an additional 0.5 equivalents of the chalcogen.

The doped structures were generated by substituting a single Sn or Ch atom in $1 \times 3 \times 3$ supercells of the $Pnma$ structures (72 atoms), and single cells of the larger π structures (64 atoms), equivalent to 2.8 and 3.1 at.% respectively. These are in line with the heavier doping levels targeted in experiments on the tin chalcogenides.^{7,13,15,16} Each model was optimised with the atomic positions allowed to relax in a fixed unit-cell geometry. The $Pnma$ supercell has a single unique Sn and Ch site, yielding a single configuration of each dopant. The π unit cell has four inequivalent Sn and Ch sites, yielding four configurations of each dopant, and we therefore quote parameters for these models as an average and range.

Finally, as a simple check on our values, we calculated formation energies E_f for the metal chalcogenides, including $Pnma$ SnS and $SnSe$, and compared them to the E_f predicted by the Materials Project^{17,18} and to experimental formation enthalpies where available.¹⁹⁻²⁵ The E_f are calculated as follows:



Initial structures of the reference elemental metals and metal chalcogenides/halides required for these calculations were obtained from the Materials Project database,¹⁸ by selecting the closest experimentally-reported structures to the convex hull, and fully optimised. The optimisations used a similar technical setup to the calculations on $Pnma$ and π SnS and $SnSe$ ²⁶, including a consistent 600 eV plane-wave cutoff and the same Sn, S and Se projector augmented-wave (PAW) pseudopotentials.^{27,28} Appropriate k -point meshes were determined by explicit convergence testing and are listed in Table S2, and PAW pseudopotentials were used with the following valence configurations: Na - $2p^6 3s^1$, Ag - $4s^2 3d^9$, Cl - $3s^2 3p^5$, Br - $4s^2 4p^5$, Sb - $5s^2 5p^3$, Bi - $6s^2 4d^{10} 6p^3$. The doped models of $Pnma$ and π SnS and $SnSe$ were generated using our in-house Transformer code.²⁹

Table S1 Electronic band gaps E_g and high frequency dielectric constants ϵ_∞ of π SnS and SnSe calculated from self-consistent ("SCF") and non self-consistent HSE06 calculations ("NSCF")^{30,31} using Γ -centered Monkhorst-Pack k -point meshes³² with up to $5 \times 5 \times 5$ subdivisions. Note that the E_g shown here are the minimum bandgaps, which correspond to indirect gaps very close to the direct gaps quoted in the text.

	k -points	π SnS		π SnSe	
		E_g [eV]	ϵ_∞	E_g [eV]	ϵ_∞
SCF	$2 \times 2 \times 2$	1.71	-	1.37	-
	$3 \times 3 \times 3$	1.67	-	1.34	-
	$4 \times 4 \times 4$	1.63	-	1.30	-
NSCF	$2 \times 2 \times 2$	1.70	14.0	1.36	18.2
	$3 \times 3 \times 3$	1.66	14.5	1.33	19.0
	$4 \times 4 \times 4$	1.61	14.7	1.28	19.3
	$5 \times 5 \times 5$	1.62	14.7	1.28	19.5

Table S2 List of reference compounds used in the doping energy calculations on π SnS and SnSe. For each compound, we list the Materials Project (MP) database identifier (mp-ID)¹⁸ crystallographic spacegroup, number of formula units in the primitive (prim.) and conventional (conv.) unit cells, k -point sampling mesh determined from convergence tests, and optimised lattice constants a , b and c , cell angles α , β and γ , and unit-cell volume V . Data for $Pnma$ SnS and SnSe was taken from our previous work.²⁶ For structures where the primitive and conventional cells differ, the k -point meshes are given in terms of the primitive cell and the lattice parameters are given in terms of the conventional cell. ^a The $R\bar{3}m$ spacegroup reported in experiments, and the $Pm\bar{3}m$ spacegroup reported in the MP database and experiments, are recovered with loose symmetry tolerances of 0.1 and 1 Å respectively.^{33,34} ^b The initial MP and optimised structures have a higher-symmetry $P2_1/c$ spacegroup than the $P2_1$ spacegroup reported for mp-31053. The structure and spacegroup match another entry, mp-610517, which is also derived from an experimental structure and is predicted to be only <30 meV higher in energy.

	mp-ID	Spacegroup	# F.U.		k -points	a [Å]	b [Å]	c [Å]	α [°]	β [°]	γ [°]	V [Å ³]
			Prim.	Conv.								
Sn	mp-117	$Fd\bar{3}m$	2	8	$6 \times 6 \times 6$	6.570			90			283.6
S	mp-77	$Fddd$	32	128	$2 \times 2 \times 2$	10.768	13.135	24.898	90			3522
Se	mp-570481	$P2_1/c$	64		$1 \times 1 \times 2$	15.318	14.785	9.446	90	93.47		2135
SnS ($Pnma$) ²⁶	-	$Pnma$	4		$4 \times 8 \times 8$	11.0	3.965	4.202	90			183.2
SnSe ($Pnma$) ²⁶	-	$Pnma$	4		$4 \times 8 \times 8$	11.35	4.124	4.335	90			202.9
Na	mp-10172	$P6_3/mmc$	2		$3 \times 3 \times 1$	3.689		6.269	90		120	73.88
Ag	mp-8566	$P6_3/mmc$	4		$17 \times 17 \times 4$	2.911	2.911	9.464	90		120	69.46
SnCl ₂	mp-29179	$P4/mmm$	8		$1 \times 4 \times 1$	9.630	4.325	15.984	90			665.7
SnBr ₂	mp-29862	$P4/mmm$	4		$3 \times 1 \times 1$	4.240	8.765	10.701	90			397.6
Sb	mp-104	$R\bar{3}m$	2	6	$6 \times 6 \times 6$	4.354	4.354	11.490	90			188.6
Bi ^a	mp-567597	$P2_1/m$	4		$4 \times 5 \times 3$	4.658	4.526	6.521	90			137.3
Na ₂ S	mp-648	$Fm\bar{3}m$	1	4	$4 \times 4 \times 4$	6.498			90			274.4
Na ₂ Se	mp-1266	$Fm\bar{3}m$	1	4	$4 \times 4 \times 4$	6.760			90			308.9
Ag ₂ S ^b	mp-31053	$P2_1/c$	4		$5 \times 2 \times 2$	4.361	7.402	8.150	90	110.39		246.6
Ag ₂ Se	mp-568936	$P2_12_12_1$	4		$4 \times 2 \times 2$	4.449	7.076	7.663				241.3
Sb ₂ S ₃	mp-2809	$Pnma$	4		$1 \times 3 \times 1$	11.800	3.845	11.367				515.7
Sb ₂ Se ₃	mp-2160	$Pnma$	4		$1 \times 3 \times 1$	12.362	4.002	11.714				579.4
Bi ₂ S ₃	mp-22856	$Pnma$	4		$2 \times 6 \times 2$	11.594	3.998	11.161				517.3
Bi ₂ Se ₃	mp-541837	$R\bar{3}m$	1	2	$5 \times 5 \times 5$	4.191	4.191	29.929	90		120	455.3

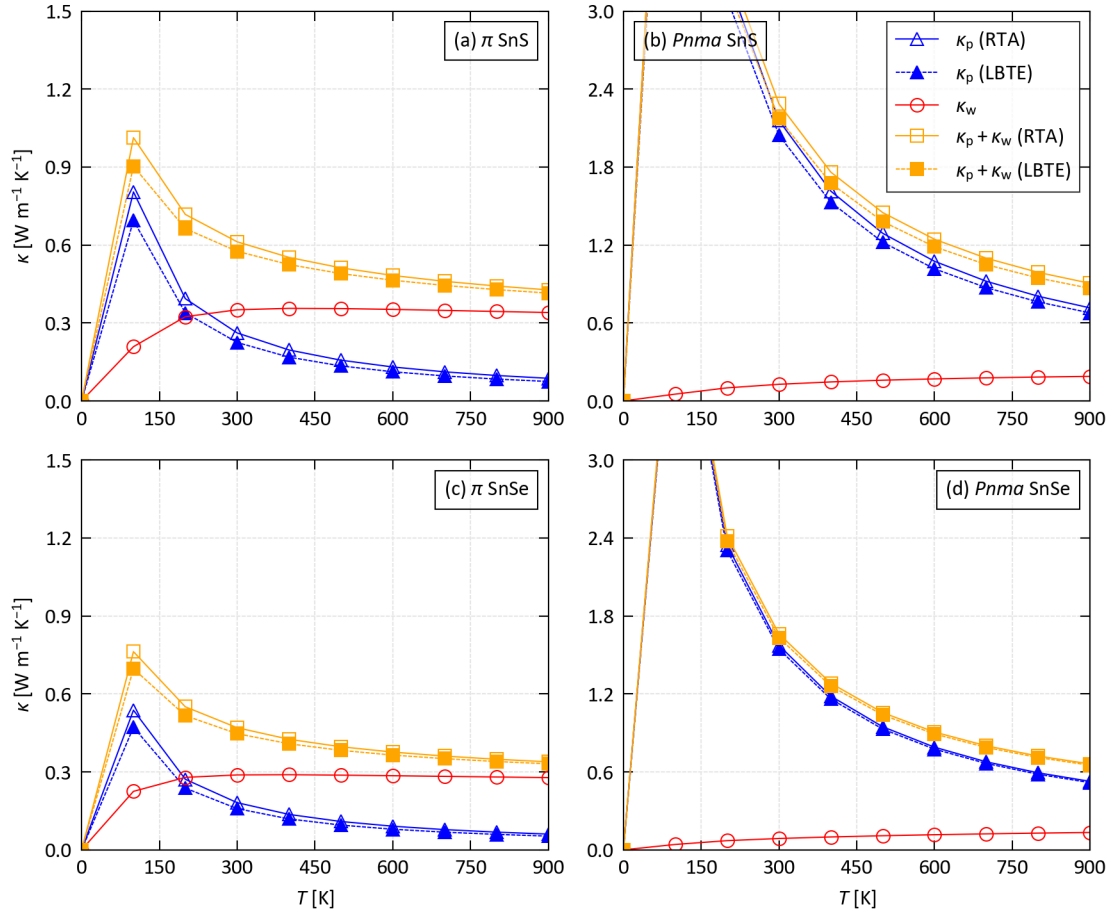


Fig. S1 Contribution of “particle-like” and “wave-like” transport κ_p/κ_w to the total lattice thermal conductivity κ_{lat} of (a) *Pnma* and (b) π SnS, and (c) *Pnma* and (d) π SnSe. On each plot, the κ_p and corresponding $\kappa_p + \kappa_w$ obtained from the single-mode relaxation-time approximation (“RTA”) and full solution of the linearised Boltzmann transport equation (“LBTE”) are shown by hollow and filled markers, respectively. (Note that the κ_w is the same for both κ_p calculations.)

2 Structure, dynamics and lattice thermal conductivity

Table S3 Nearest-neighbour tin-chalcogen distances $d_{\text{Sn-Ch}}$ in $Pnma$ and π SnS and SnSe. The second column shows the number of symmetry-equivalent sites in each chemical environment, and where applicable the numbers of equivalent distances are indicated in parentheses.

	n_s	$d_{\text{Sn-Ch}} [\text{\AA}]$		
		d_1	d_2	d_3
SnS ($Pnma$)	4	2.632	2.661 (2)	-
	4	2.651 (3)	-	-
SnS (π)	12	2.613	2.634	2.677
	4	2.654 (3)	-	-
	12	2.617	2.638	2.710
SnSe ($Pnma$)	4	2.759	2.790 (2)	-
	4	2.786 (3)	-	-
SnSe (π)	12	2.741	2.766	2.823
	4	2.786	-	-
	12	2.749 (3)	2.764	2.843

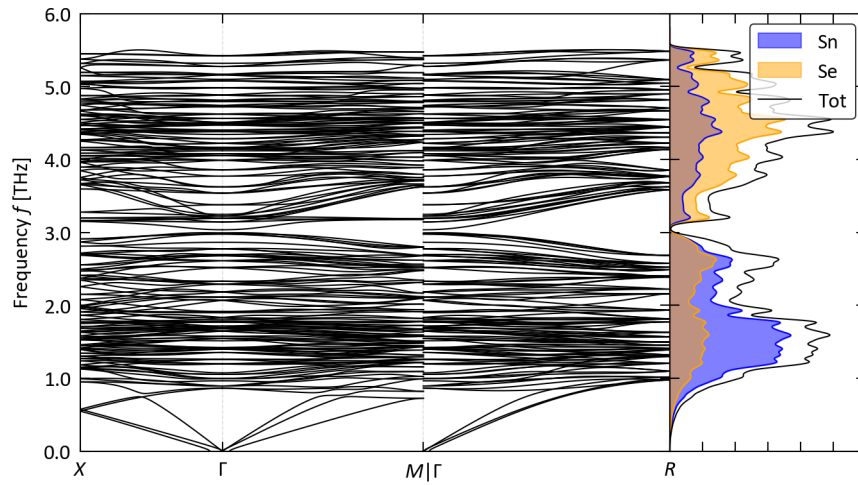


Fig. S2 Phonon dispersion and density of states (DoS) of π SnSe. The blue and orange shaded regions show the projections of the DoS onto the Sn and Se atoms, respectively.

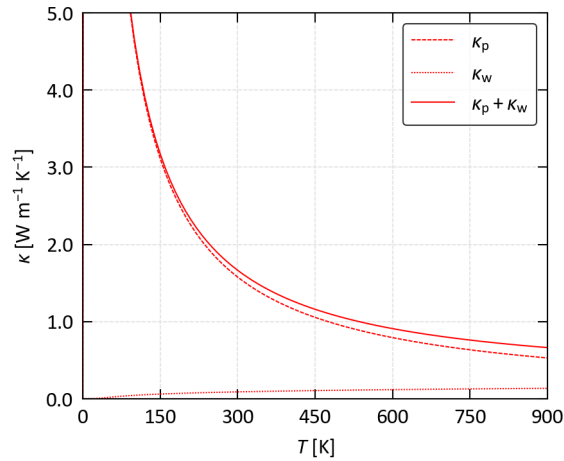


Fig. S3 Contribution of "particle-like" and "wave-like" transport κ_p/κ_w to the total lattice thermal conductivity κ_{latt} of $Pnma$ SnSe.

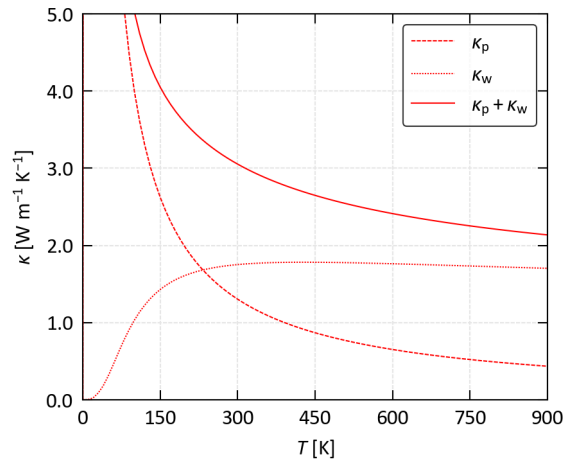


Fig. S4 Contribution of “particle-like” and “wave-like” transport κ_p/κ_w to the total lattice thermal conductivity κ_{latt} of π SnS.

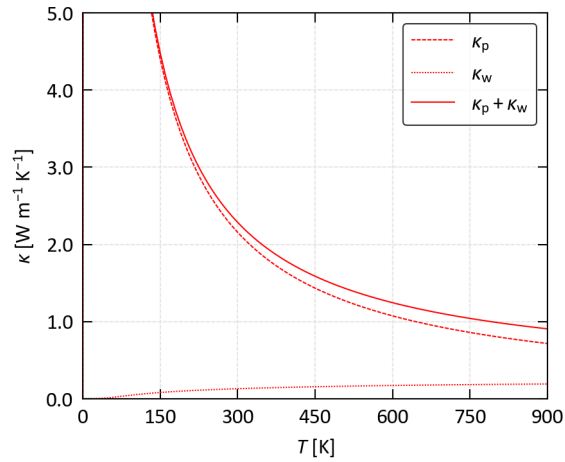


Fig. S5 Contribution of “particle-like” and “wave-like” transport κ_p/κ_w to the total lattice thermal conductivity κ_{latt} of *Pnma* SnS.

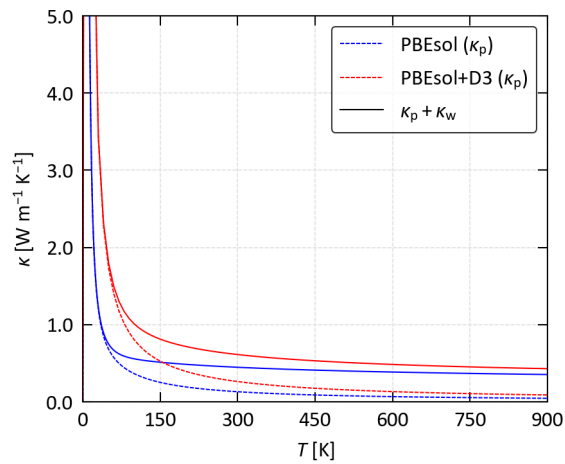


Fig. S6 Comparison of the “particle-like” lattice thermal conductivity κ_p and total conductivity $\kappa_{\text{latt}} = \kappa_p + \kappa_w$ of π SnS obtained with the PBEsol functional³⁵ and the PBEsol+D3 exchange-correlation treatment used in the present study.

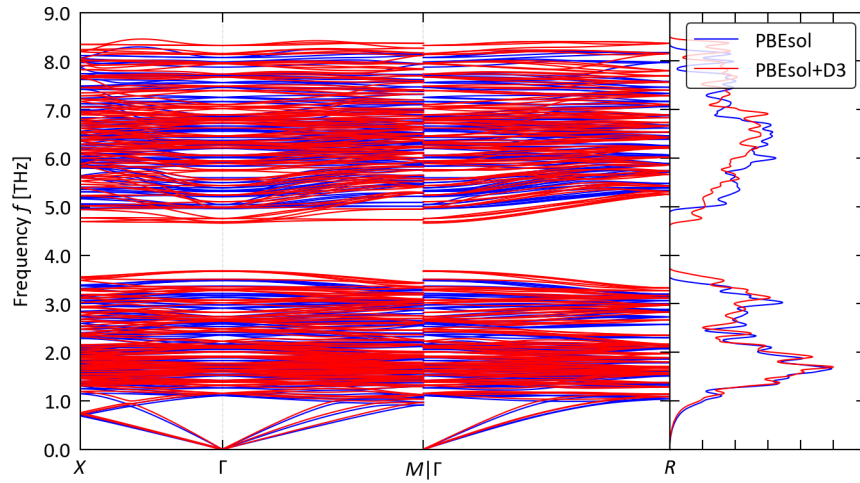


Fig. S7 Comparison of the phonon dispersion and density of states (DoS) of π SnS obtained with the PBEsol functional³⁵ and the PBEsol+D3 exchange-correlation treatment used in the present study.

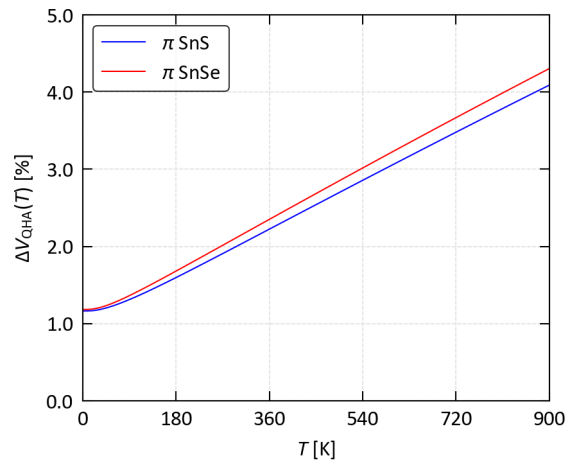


Fig. S8 Predicted thermal expansion of π SnS and SnSe as a function of temperature, relative to the optimised “athermal” equilibrium unit-cell volume V_0 , obtained from the quasi-harmonic phonon calculations reported in Ref.²⁶.

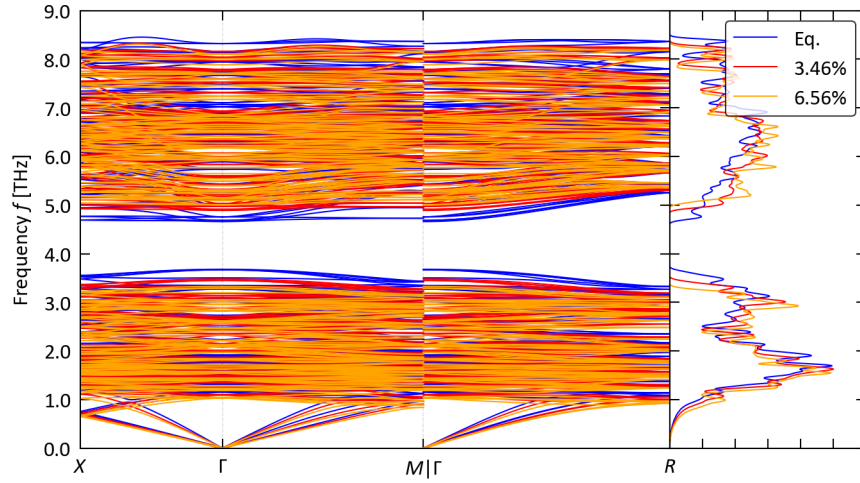


Fig. S9 Comparison of the phonon dispersion and density of states (DoS) of π SnS calculated at the “athermal” equilibrium unit-cell volume V_0 and volumes corresponding to 3.46 and 6.56% expansions. Data for the calculations at the expanded volumes is taken from our previous work.²⁶

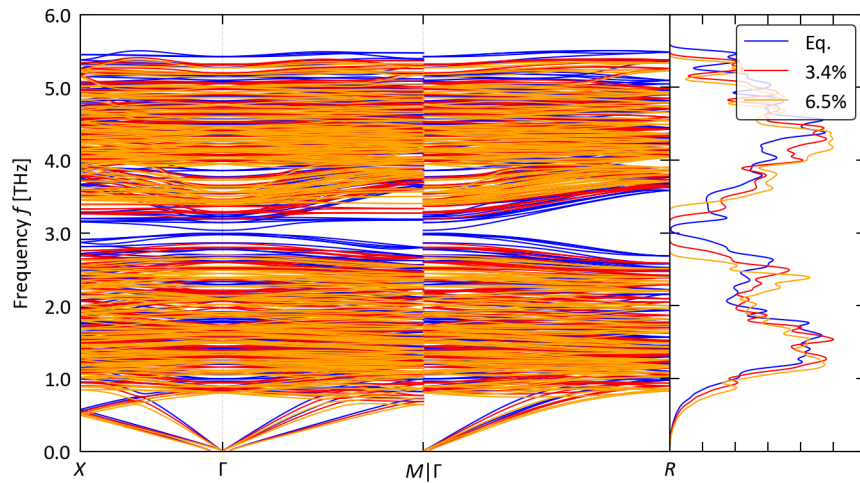


Fig. S10 Comparison of the phonon dispersion and density of states (DoS) of π SnSe calculated at the “athermal” equilibrium unit-cell volume V_0 and volumes corresponding to 3.4 and 6.5% expansions. Data for the calculations at the expanded volumes is taken from our previous work.²⁶

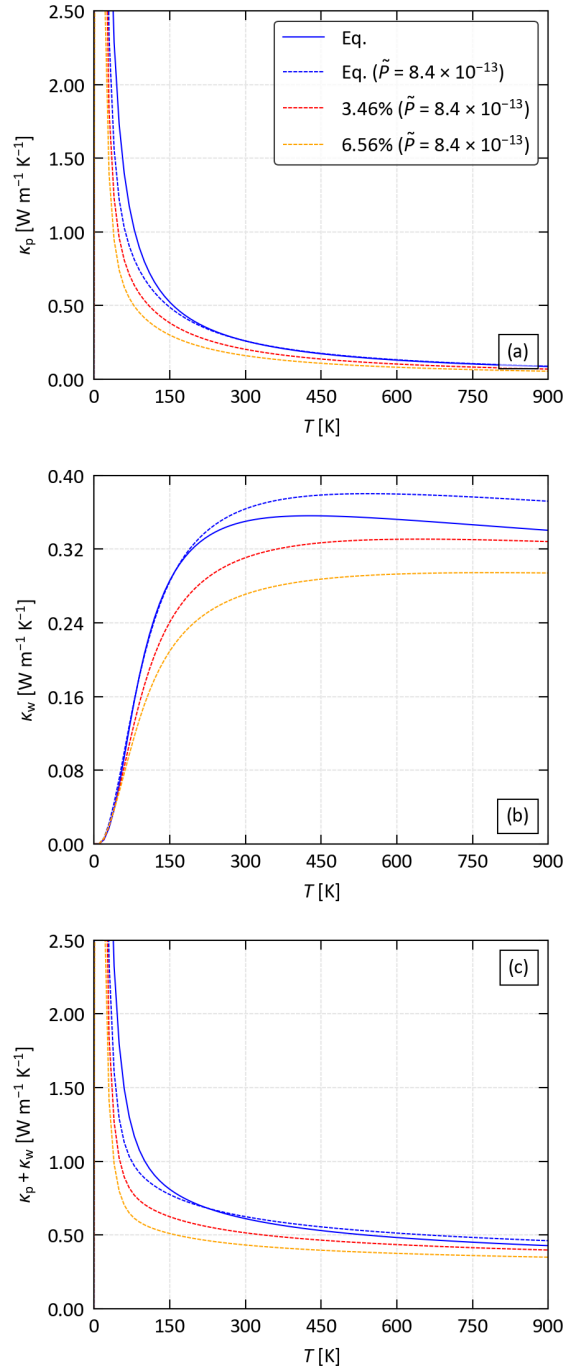


Fig. S11 Predicted “particle-like”, “wave-like” and total lattice thermal conductivity, κ_p , κ_w and $\kappa_p + \kappa_w$ of π SnS as a function of temperature. The predicted κ_{att} obtained at the “athermal” equilibrium unit-cell volume V_0 shown in the text is compared to calculations performed using a constant averaged three-phonon interaction strength $\tilde{P} = 8.363 \times 10^{-13} \text{ eV}^2$ and harmonic phonon spectra obtained at $V = V_0$ and volume expansions corresponding to 3.46 and 6.56% expansions (see Section 1.4).

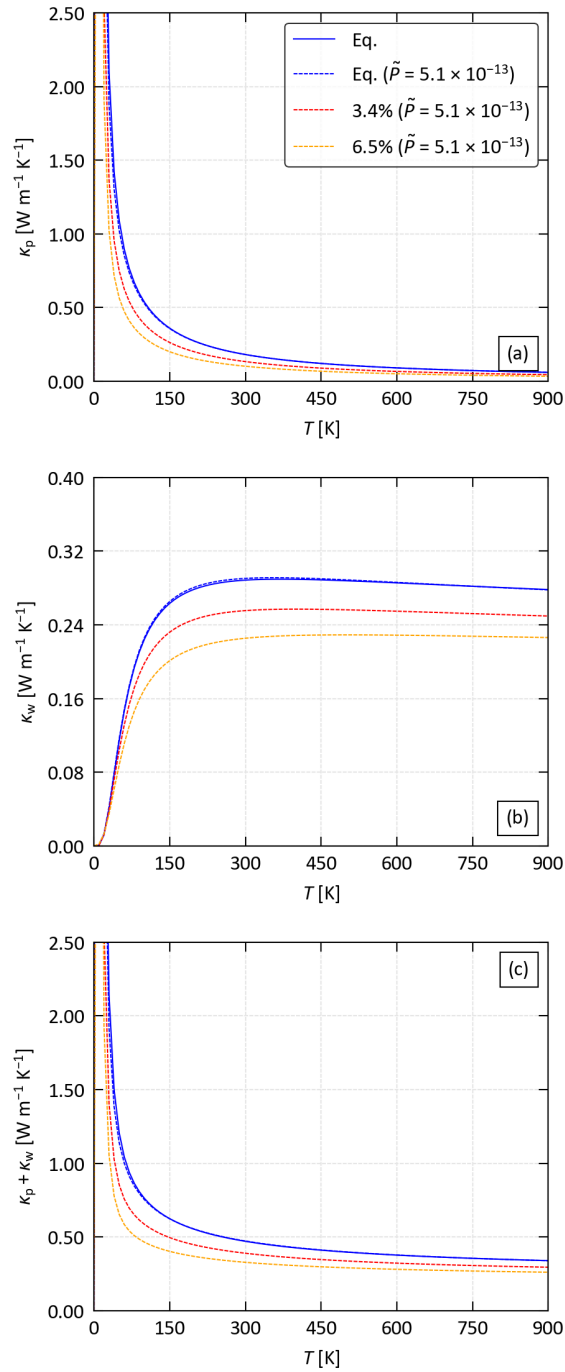


Fig. S12 Predicted “particle-like”, “wave-like” and total lattice thermal conductivity, κ_p , κ_w and $\kappa_p + \kappa_w$ of π SnSe as a function of temperature. The predicted κ_{latt} obtained at the “athermal” equilibrium unit-cell volume V_0 shown in the text is compared to calculations performed using a constant averaged three-phonon interaction strength $\tilde{P} = 5.111 \times 10^{-13} \text{ eV}^2$ and harmonic phonon spectra obtained at $V = V_0$ and volume expansions corresponding to 3.46 and 6.56% expansions (see Section 1.4).

3 Electrical transport

Table S4 Calculated scalar-average electrical conductivity σ and Seebeck coefficient S determined within the constant relaxation-time approximation with $\tau^{el} = 10^{-14} \text{ s}^{-1}$ for p- and n-type $Pnma$ and π SnS/SnSe, together with the effective potential η_{eff} , conductivity and Seebeck effective masses m_{σ}^*/m_S^* , and Fermi surface complexity factor $N_V^*K^*$ determined using the approach outlined in Ref. ⁸.

		σ [S cm^{-1}]	S [$\mu\text{V K}^{-1}$]	η_{eff}	m_{σ}^* [m_e]	m_S^* [m_e]	$N_V^*K^*$
SnS ($Pnma$)	p-type	441	245	-0.01	0.26	0.7	4.56
	n-type	625	-250	-0.09	0.18	0.73	8.20
SnS (π)	p-type	67.2	397	-2.05	1.68	2.36	1.67
	n-type	97.9	-405	-2.15	1.15	2.52	3.24
SnSe ($Pnma$)	p-type	411	263	-0.28	0.27	0.81	5.11
	n-type	750	-252	-0.12	0.15	0.75	11.05
SnSe (π)	p-type	44.6	410	-2.22	2.53	2.63	1.06
	n-type	99.7	-414	-2.26	1.13	2.71	3.70

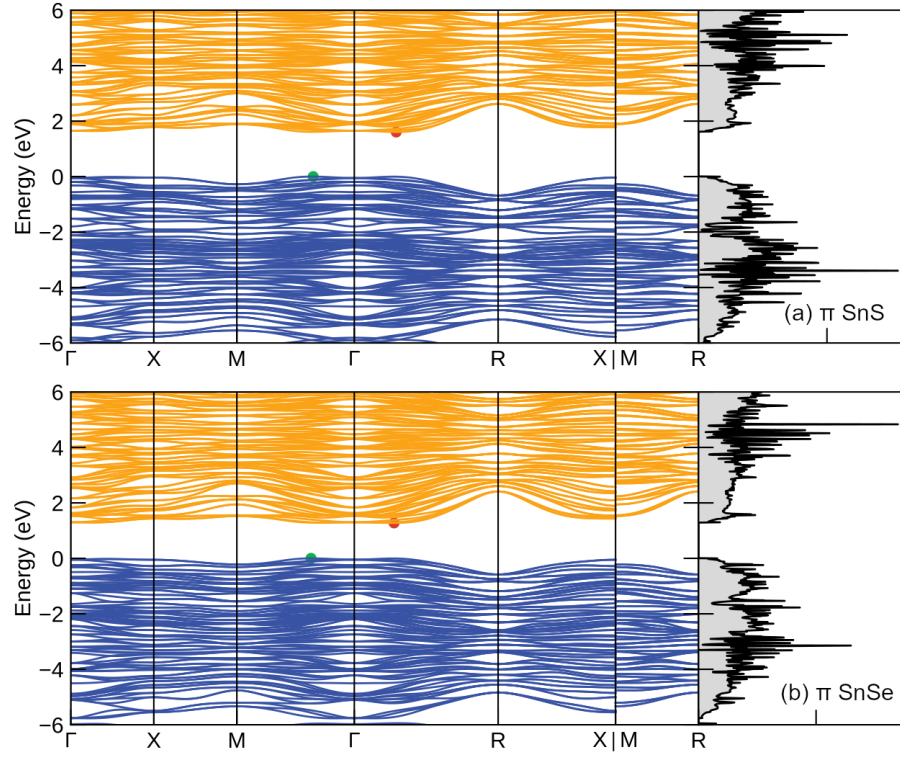


Fig. S13 Electronic band structures and density of states (DoS) of π SnS (a) and π SnSe (b) obtained from non-self-consistent HSE06 calculations. ^{30,31} On each band structure, the valence and conduction bands are shown in blue and orange lines, respectively, the valence-band maxima and conduction-band minima (VBM/CBM) are marked by green and red circles, and the VBM is set to 0 eV.

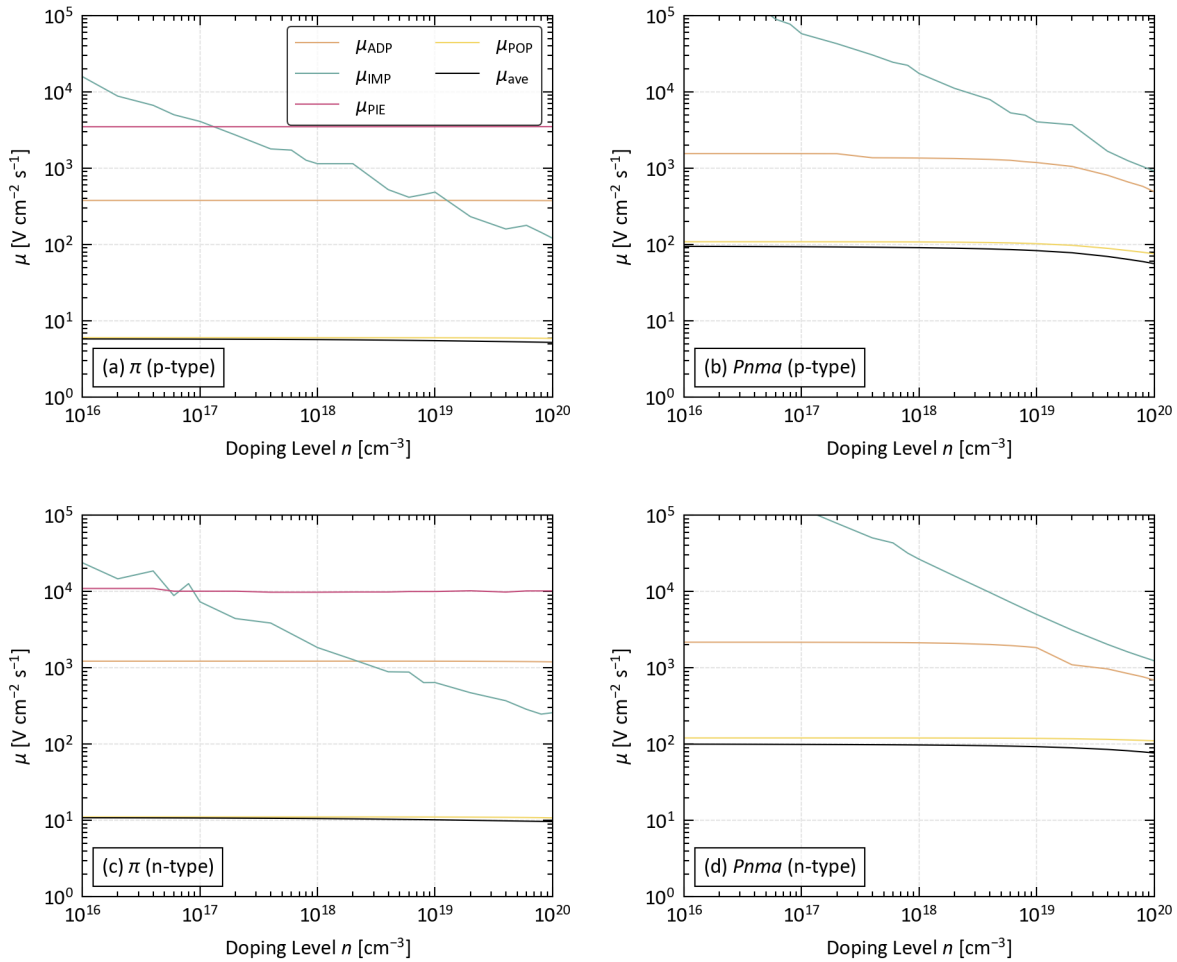


Fig. S14 Calculated (a)/(b) hole and (c)/(d) electron mobility μ as a function of extrinsic carrier concentration n (“doping level”) at $T = 700 \text{ K}$ for (a)/(c) π SnS and (b)/(d) $Pnma$ SnS. The overall mobility μ_{total} is shown in black together with the mobilities from the four carrier scattering mechanisms modelled in the calculations, viz. acoustic deformation potential (μ_{ADP} , orange), polar-optic phonon (μ_{POP} , yellow), ionised impurity (μ_{IMP} , green), and piezoelectric (μ_{PIE} , red). Note that piezoelectric scattering is not relevant to $Pnma$ SnS due to the centrosymmetric crystal structure.

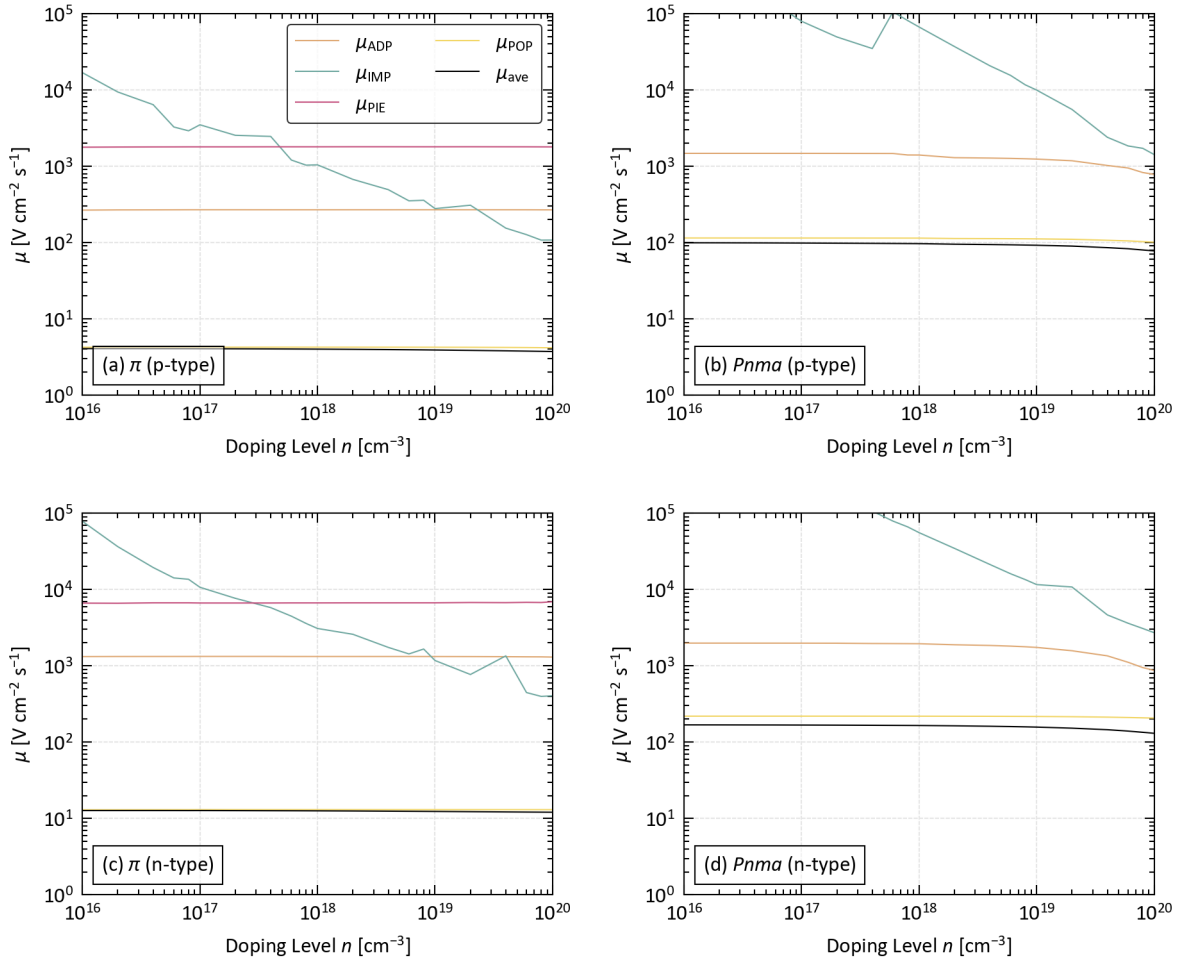


Fig. S15 Calculated (a)/(b) hole and (c)/(d) electron mobility μ as a function of extrinsic carrier concentration n ("doping level") at $T = 700 \text{ K}$ for (a)/(c) π SnSe and (b)/(d) $Pnma$ SnSe. The overall mobility μ_{total} is shown in black together with the mobilities from the four carrier scattering mechanisms modelled in the calculations, viz. acoustic deformation potential (μ_{ADP} , orange), polar-optic phonon (μ_{POP} , yellow), ionised impurity (μ_{IMP} , green), and piezoelectric (μ_{PIE} , red). Note that piezoelectric scattering is not relevant to $Pnma$ SnSe due to the centrosymmetric crystal structure.

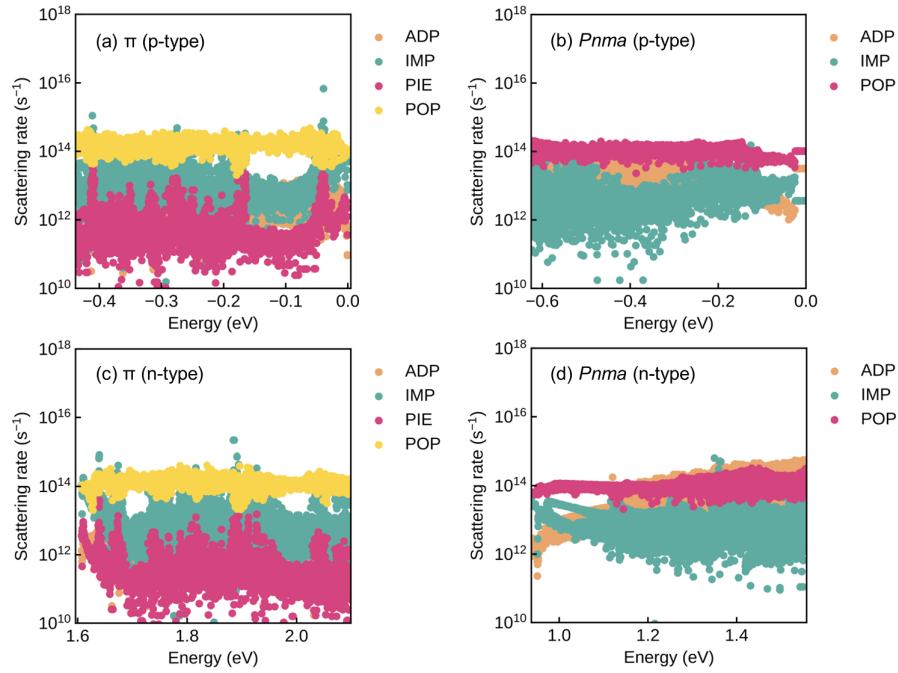


Fig. S16 Calculated scattering rates as a function of energy for (a)/(c) π SnS and (b)/(d) $Pnma$ SnS in the vicinity of the (a)/(b) valence and (c)/(d) conduction band edges at a doping level of $n = 4 \times 10^{19} \text{ cm}^{-3}$ and temperature $T = 700 \text{ K}$. Scattering rates for the four carrier scattering mechanisms modelled in the calculations are shown, *viz.* acoustic deformation potential (ADP), polar-optic phonon (POP), ionised impurity (IMP), and piezoelectric (PIE). Note that piezoelectric scattering is not relevant to $Pnma$ SnS due to the centrosymmetric crystal structure, and that the colours for the different rates are different in the plots for the π and $Pnma$ phases.

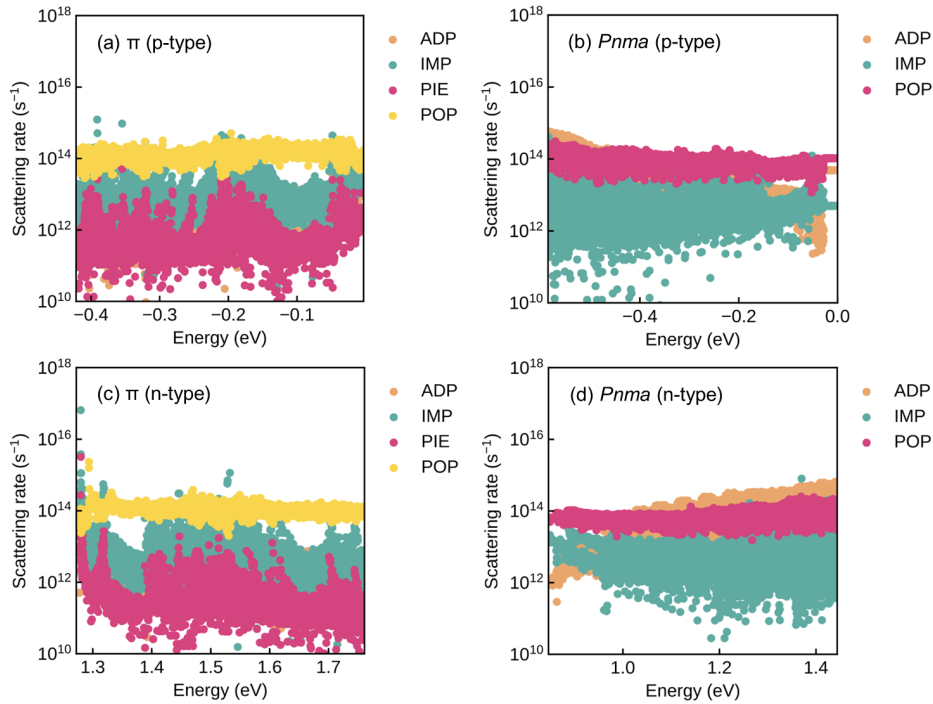


Fig. S17 Calculated scattering rates as a function of energy for (a)/(c) π SnSe and (b)/(d) $Pnma$ SnSe in the vicinity of the (a)/(b) valence and (c)/(d) conduction band edges at a doping level of $n = 4 \times 10^{19} \text{ cm}^{-3}$ and temperature $T = 700 \text{ K}$. Scattering rates for the four carrier scattering mechanisms modelled in the calculations are shown, *viz.* acoustic deformation potential (ADP), polar-optic phonon (POP), ionised impurity (IMP), and piezoelectric (PIE). Note that piezoelectric scattering is not relevant to $Pnma$ SnSe due to the centrosymmetric crystal structure, and that the colours for the different rates are different in the plots for the π and $Pnma$ phases.

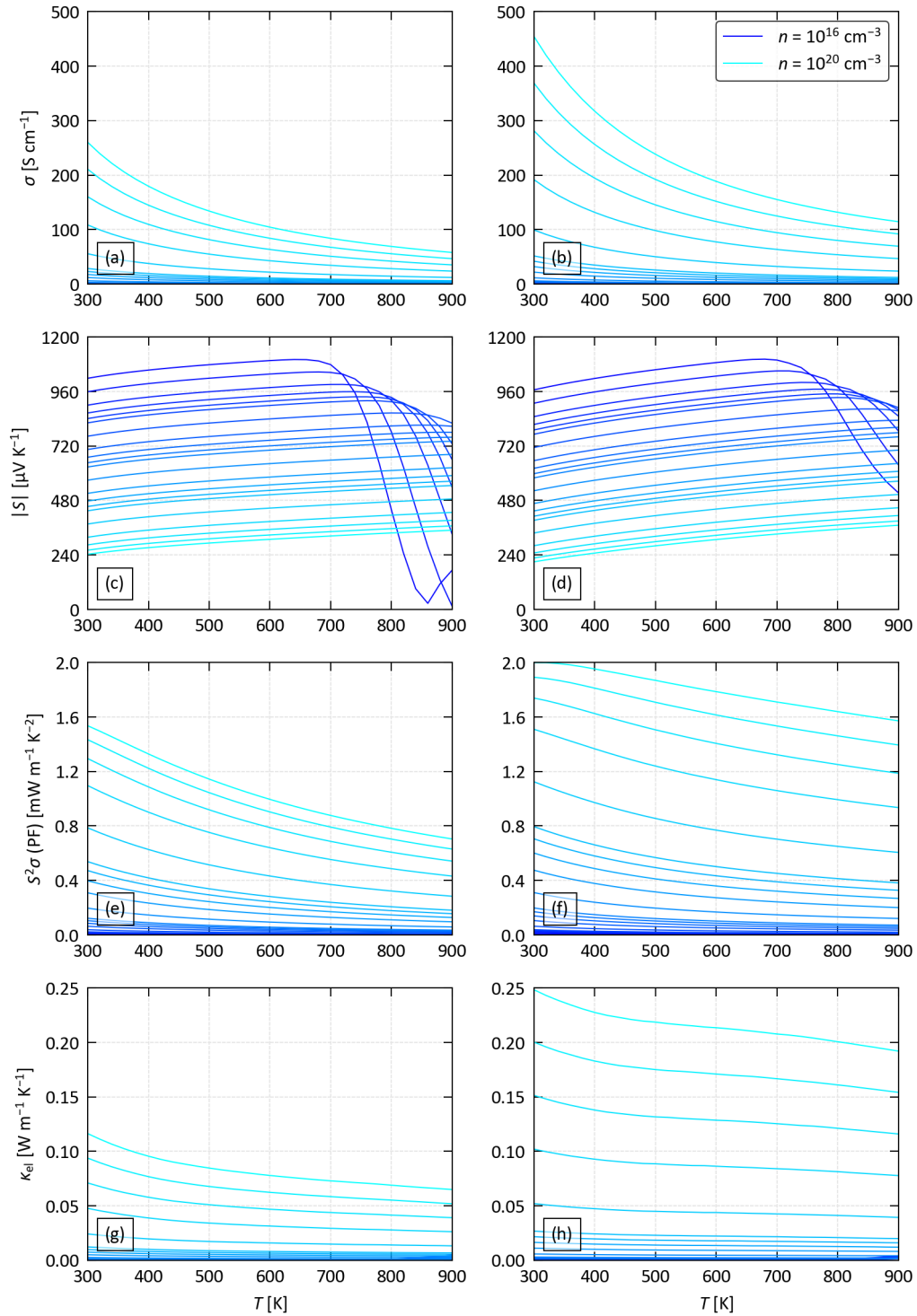


Fig. S18 Calculated electrical properties of π SnS as a function of temperature with extrinsic carrier concentrations n between 10^{16} - 10^{20} cm^{-3} : (a)/(b) electrical conductivity σ , (c)/(d) absolute Seebeck coefficient $|S|$, (e)/(f) power factor $S^2\sigma$ (PF), and (g)/(h) electronic thermal conductivity κ_{el} . The colour scale for the lines runs between blue ($n = 10^{16}$ cm^{-3}) and cyan ($n = 10^{20}$ cm^{-3}). The left-hand column ((a), (c), (e), (g)) shows the electrical properties with p-type doping, and the right-hand column ((b), (d), (f), (h)) shows the properties with n-type doping.

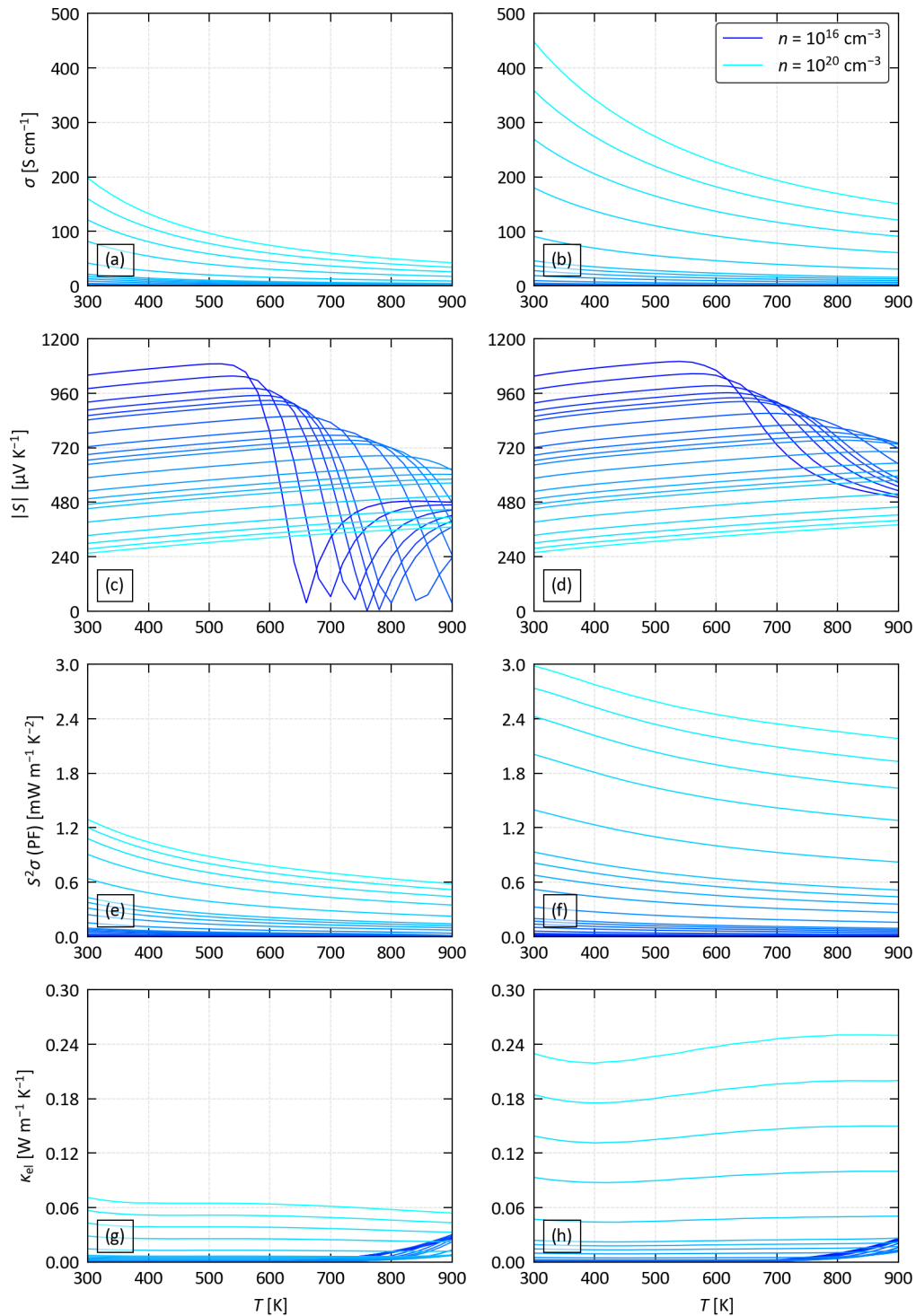


Fig. S19 Calculated electrical properties of π SnSe as a function of temperature with extrinsic carrier concentrations n between 10^{16} - 10^{20} cm^{-3} : (a)/(b) electrical conductivity σ , (c)/(d) absolute Seebeck coefficient $|S|$, (e)/(f) power factor $S^2\sigma$ (PF), and (g)/(h) electronic thermal conductivity κ_{el} . The colour scale for the lines runs between blue ($n = 10^{16}$ cm^{-3}) and cyan ($n = 10^{20}$ cm^{-3}). The left-hand column ((a), (c), (e), (g)) shows the electrical properties with p-type doping, and the right-hand column ((b), (d), (f), (h)) shows the properties with n-type doping.

4 Thermoelectric figure of merit

Table S5 Calculated maximum thermoelectric figure of merit ZT_{\max} of π and $Pnma$ SnS and SnSe with corresponding temperature T , doping level n , and associated electrical conductivity σ , Seebeck coefficient S , power factor $S^2\sigma$ (PF), and electronic, lattice and total thermal conductivity κ_{el} , κ_{latt} and κ_{tot} . Values are calculated at maximum temperatures of $T = 880$ and 800 K, close to the phase transition temperatures of the orthorhombic phases.³⁶ For π SnS and SnSe, we provide ZT_{\max} at $n = 4 \times 10^{19}$ and 10^{20} cm^{-3} , which are the maximum n achieved in experiments on the p-type orthorhombic phases^{9,15} and the maximum tested in our calculations, respectively. Data for $Pnma$ SnS and SnSe are taken from our previous work,^{3,37,38} but the κ_{latt} has been recalculated to include the intraband tunnelling contribution κ_w .

		n [cm^{-3}]	T [K]	ZT	σ [S cm^{-1}]	S [$\mu\text{V K}^{-1}$]	PF $S^2\sigma$ [$\text{mW m}^{-1} \text{K}^{-2}$]	κ [$\text{W m}^{-1} \text{K}^{-1}$]		
								κ_{el}	κ_{latt}	κ_{tot}
π -cubic SnS	p-type	4×10^{19}	880	0.85	24	425	0.44	0.03	0.43	0.46
	p-type	10^{20}	880	1.27	60	347	0.72	0.07	0.43	0.50
	n-type	4×10^{19}	880	1.64	48	-444	0.95	0.08	0.43	0.51
	n-type	10^{20}	880	2.24	117	-367	1.58	0.19	0.43	0.62
π -cubic SnSe	p-type	4×10^{19}	800	0.83	20	436	0.39	0.02	0.35	0.37
	p-type	10^{20}	800	1.25	50	358	0.64	0.06	0.35	0.41
	n-type	4×10^{19}	800	2.39	68	-443	1.34	0.10	0.35	0.45
	n-type	10^{20}	800	3.01	169	-365	2.26	0.25	0.35	0.60
SnS ($Pnma$) ^{3,37,38}	p-type	4×10^{19}	880	1.26	305	255	1.98	0.46	0.92	1.38
	n-type	4×10^{19}	880	1.60	386	-262	2.65	0.54	0.92	1.46
SnSe ($Pnma$) ^{3,37,38}	p-type	4×10^{19}	800	2.03	448	262	3.07	0.49	0.72	1.21
	n-type	2×10^{19}	800	2.38	400	-299	3.58	0.48	0.72	1.20

Table S6 Calculated doping energies E_d , extrinsic carrier concentrations (“doping levels”) n , and, where relevant, precipitation energies E_p for π SnS and SnSe doped with Na, Ag, Cl, Br, Bi and Sb. The E_d and E_p are defined in Eqs 20/21 and 22 in Section 1.6. The unit cell of the π phases have four crystallographically-independent Sn and chalcogen sites, so values for π SnS and SnSe are presented as an average, taking into account site degeneracy, and a range.

Dopant	Parent Phase	E_d [eV]	n [cm^{-3}]	E_p [eV]
Na	$Pnma$ SnS	-0.61	1	0.07
	π SnS	-0.45 (-0.52 to -0.37)	1 (0.99-1.03)	-0.12 (-0.2 to 0.04)
	$Pnma$ SnSe	-0.55	1	0.03
	π SnSe	-0.50 (-0.57 to -0.43)	0.01 (0.97-1.04)	-0.07 (-0.13-0)
Ag	$Pnma$ SnS	1.32	1	-0.27
	π SnS	1.53 (1.48-1.59)	0.99 (0.97-1)	-0.51 (-0.57 to -0.45)
	$Pnma$ SnSe	1.29	1	-0.36
	π SnSe	1.36 (1.3-1.43)	1.01 (1-1.03)	-0.47 (-0.55 to -0.42)
Cl	$Pnma$ SnS	1.67	-1	-
	π SnS	1.72 (1.64-1.91)	-1 (-1.01 to -0.99)	-
	$Pnma$ SnSe	1.47	-1	-
	π SnSe	1.54 (1.48-1.71)	-1 (-1.01 to -1)	-
Br	$Pnma$ SnS	1.65	-1	-
	π SnS	1.72 (1.64-1.93)	-1.01 (-1.02 to -1)	-
	$Pnma$ SnSe	1.37	-1	-
	π SnSe	1.56 (1.4-1.62)	-1.01 (-1.02 to -1)	-
Sb	$Pnma$ SnS	1.07	-1	-0.68
	π SnS	1.14 (1.09-1.2)	-1	-0.78 (-0.85 to -0.73)
	$Pnma$ SnSe	0.82	-1	-0.49
	π SnSe	0.93 (0.89-0.96)	-1.01 (-1 to -1.03)	-0.64 (-0.67 to -0.59)
Bi	$Pnma$ SnS	0.86	-1	-0.77
	π SnS	0.94 (0.91-1)	-0.99 (-0.96 to -1)	-0.88 (-0.85 to -0.93)
	$Pnma$ SnSe	0.59	-1	-0.56
	π SnSe	0.7 (0.67-0.72)	-1 (-1 to -1.02)	-0.72 (-0.69 to -0.74)

Table S7 Calculated formation energies E_f for $Pnma$ SnS and SnSe and the metal chalcogenide compounds used to determine the precipitation energies E_p in Table S6. The E_f are defined in Eq. 23 in section 1.6. For each compound, we list the Materials Project database identifier (mp-ID) and the E_f reported in the MP database^{17,18} and from experimental formation enthalpies where available.^{19–25} (Note that we were not able to find measured formation enthalpies for Na₂Se and Sb₂Se₃.)

	mp-ID	E_f [eV per F.U.]		
		This work	Materials Project	Expt
$Pnma$ SnS	mp-2231	-1.1	-0.94	-1.01/-1.09 ¹⁹
$Pnma$ SnSe	mp-691	-1.09	-0.91	-0.93 ²⁰
Na ₂ S	mp-648	-3.27	-3.81	-3.82 ²¹
Na ₂ Se	mp-1266	-3.23	-3.81	
Ag ₂ S	mp-31053	-0.09	-0.67	-0.32 ²²
Ag ₂ Se	mp-568936	-0.33	-0.65	-0.41 ²³
Sb ₂ S ₃	mp-2809	-1.43	-1.44	-1.47 ²⁴
Sb ₂ Se ₃	mp-2160	-1.51	-1.42	
Bi ₂ S ₃	mp-22856	-2.01	-3.32	-1.4 ²²
Bi ₂ Se ₃	mp-541837	-2.14	-3.45	-1.5 ²⁵

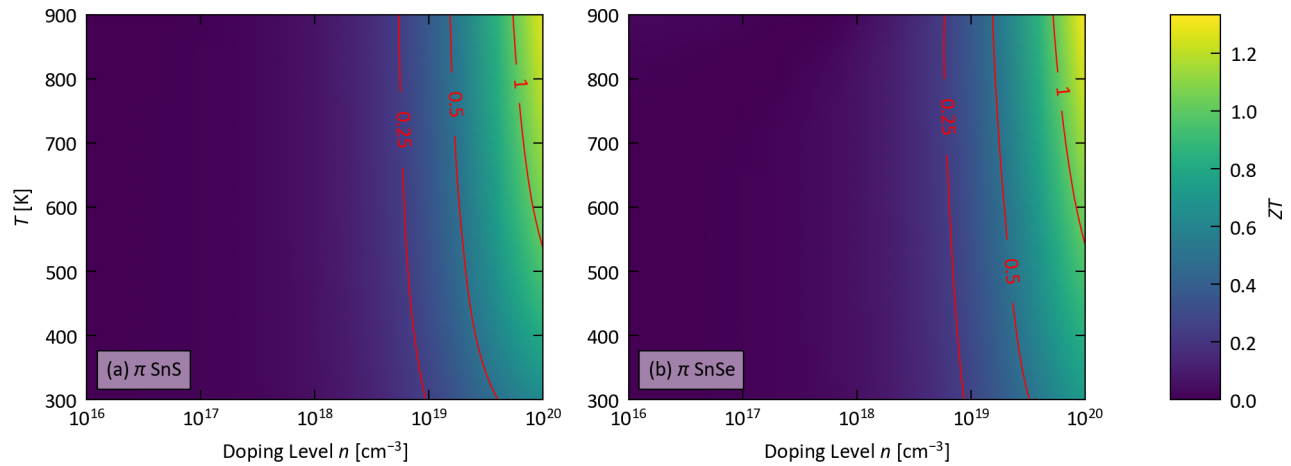


Fig. S20 Predicted thermoelectric figure of merit ZT of p-type π SnS (a) and SnSe (b) as a function of extrinsic electron carrier concentration n ("doping level") and temperature T . Values of $ZT = 0.25, 0.5$, and 1 are shown by contour lines.

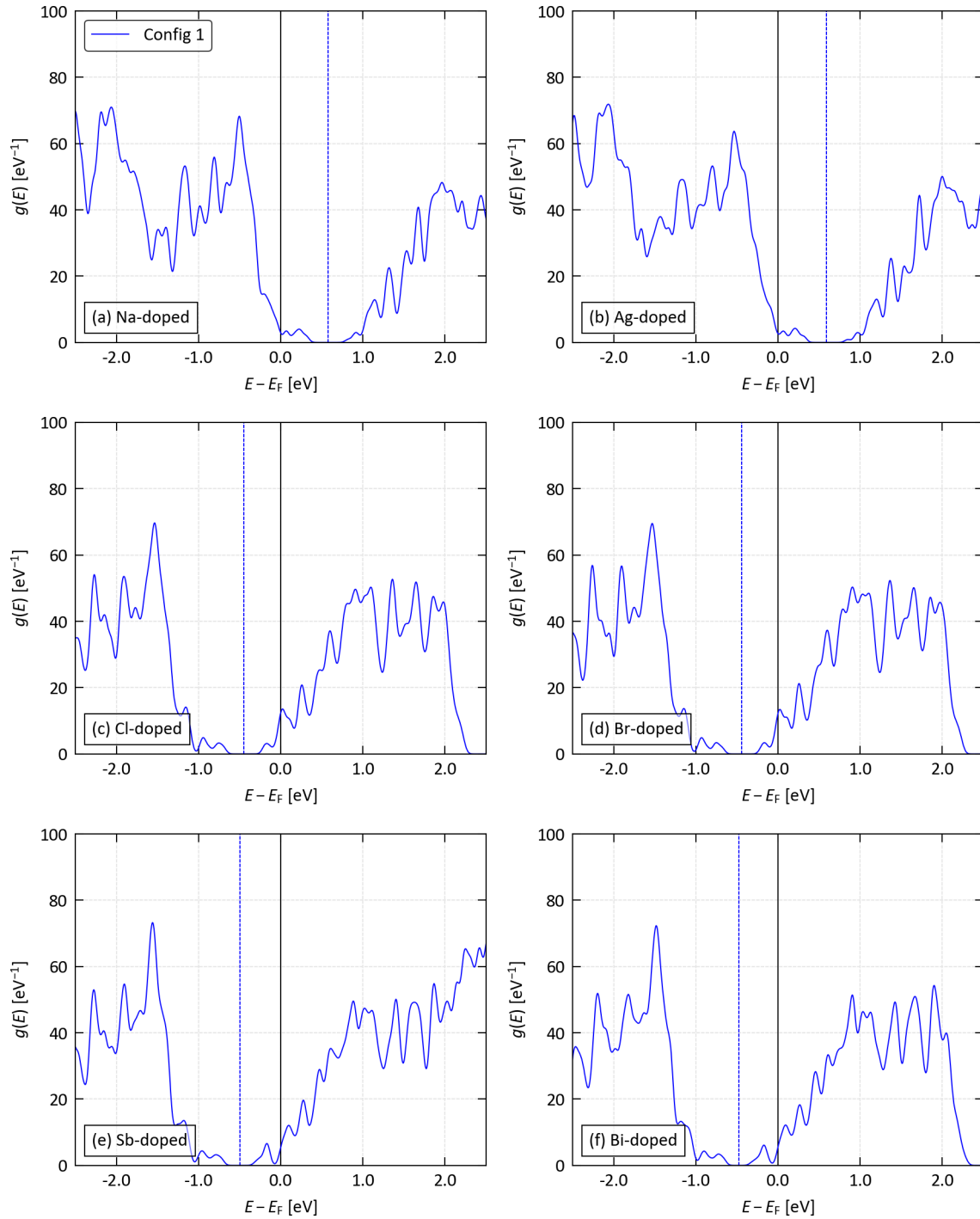


Fig. S21 Calculated electronic density of states (DoS) of *Pnma* SnS doped with Na (a), Ag (b), Cl (c), Br (d), Sb (e) and Bi (f). On each plot, the approximate midpoint of the host bandgap, used to estimate the ionisation of the dopant atom, is shown as a vertical dashed line. These calculations were performed with the PBEsol functional and the bandgaps are underestimated compared to the more accurate non-self-consistent HSE06 calculations discussed in the text.

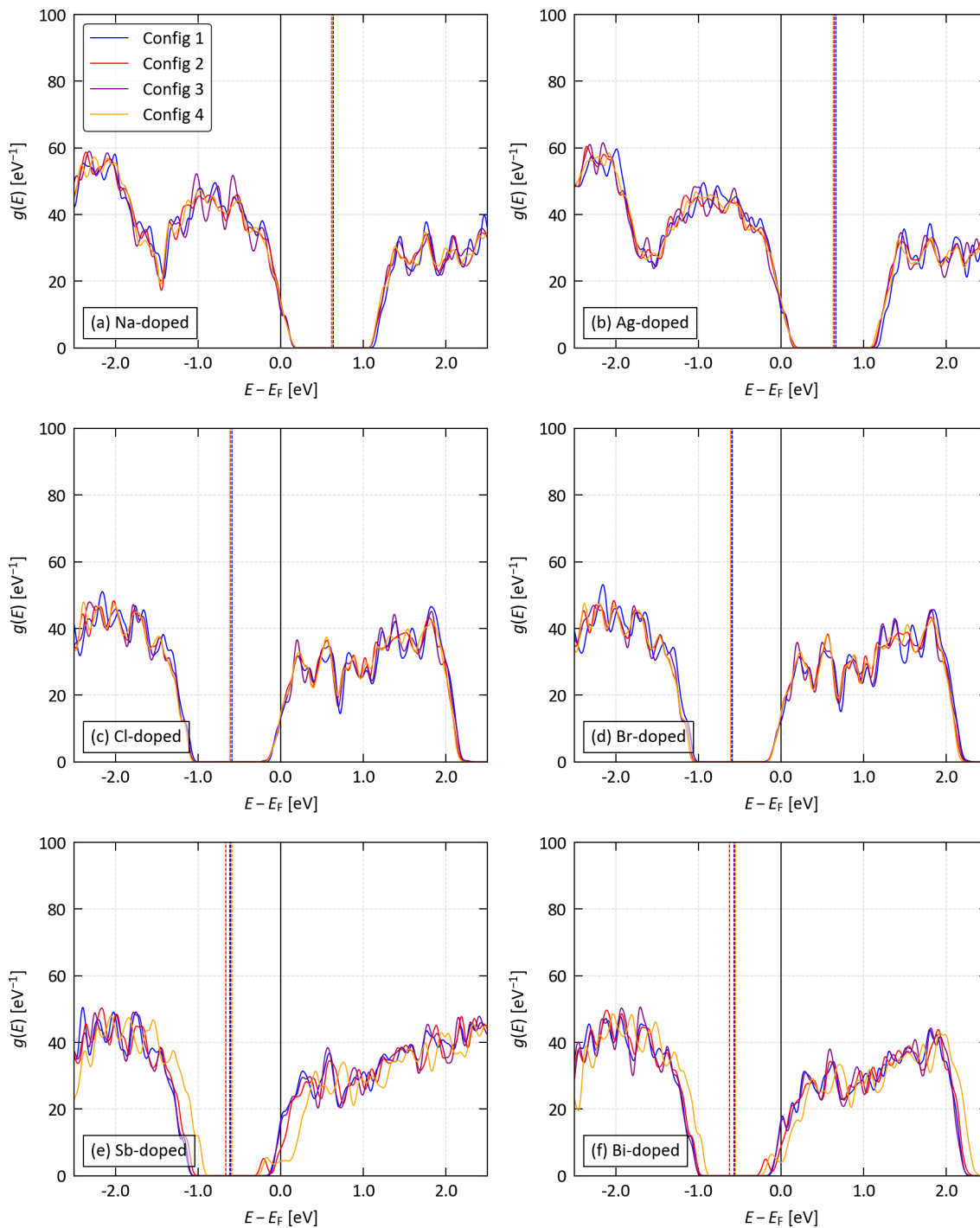


Fig. S22 Calculated electronic density of states (DoS) of π SnS doped with Na (a), Ag (b), Cl (c), Br (d), Sb (e) and Bi (f). On each plot, the approximate midpoints of the host bandgaps, used to estimate the ionisation of the dopant atom, are shown as vertical dashed lines. These calculations were performed with the PBEsol functional and the bandgaps are underestimated compared to the more accurate non-self-consistent HSE06 calculations discussed in the text.

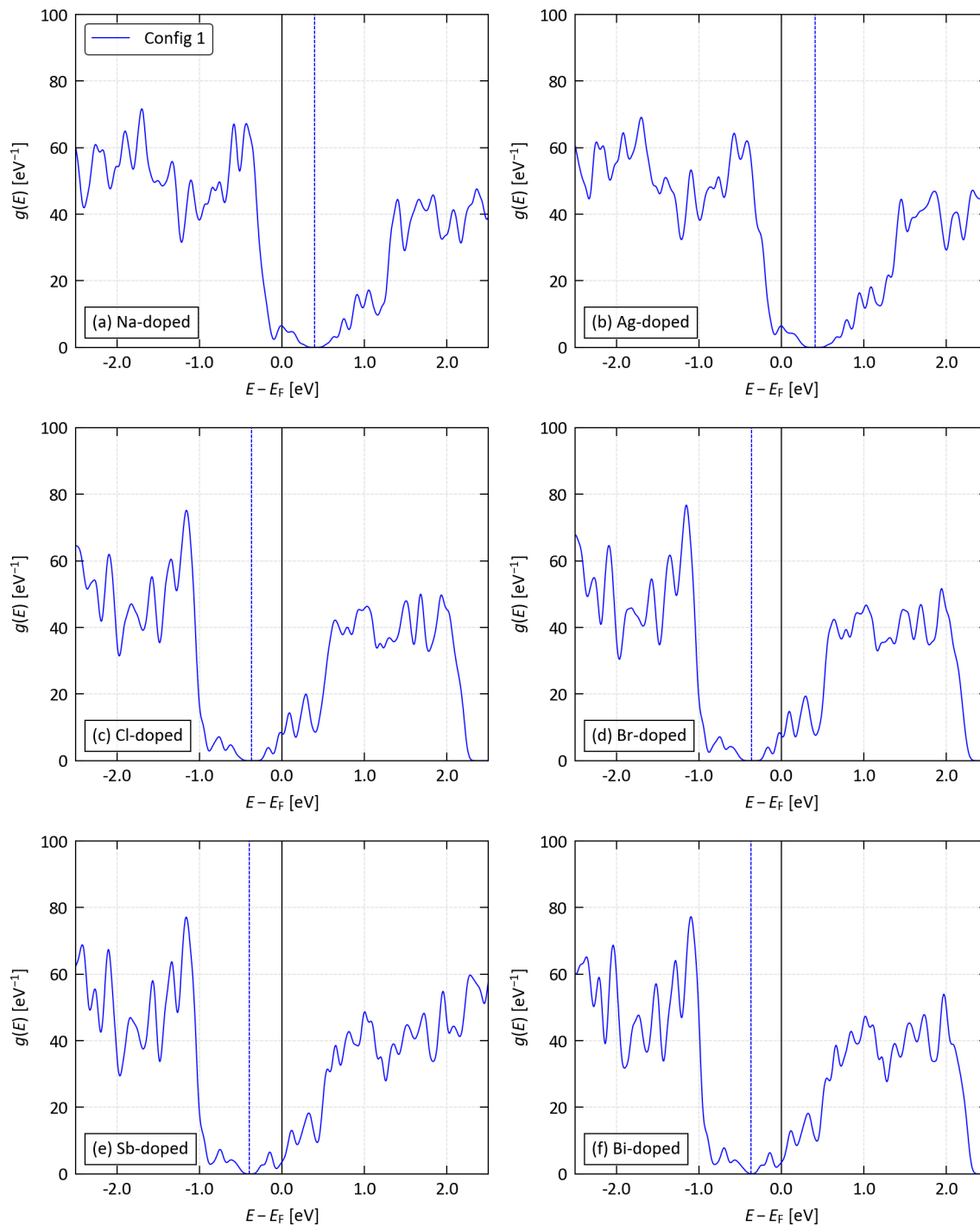


Fig. S23 Calculated electronic density of states (DoS) of *Pnma* SnSe doped with Na (a), Ag (b), Cl (c), Br (d), Sb (e) and Bi (f). On each plot, the approximate midpoint of the host bandgap, used to estimate the ionisation of the dopant atom, is shown as a vertical dashed line. These calculations were performed with the PBEsol functional and the bandgaps are underestimated compared to the more accurate non-self-consistent HSE06 calculations discussed in the text.

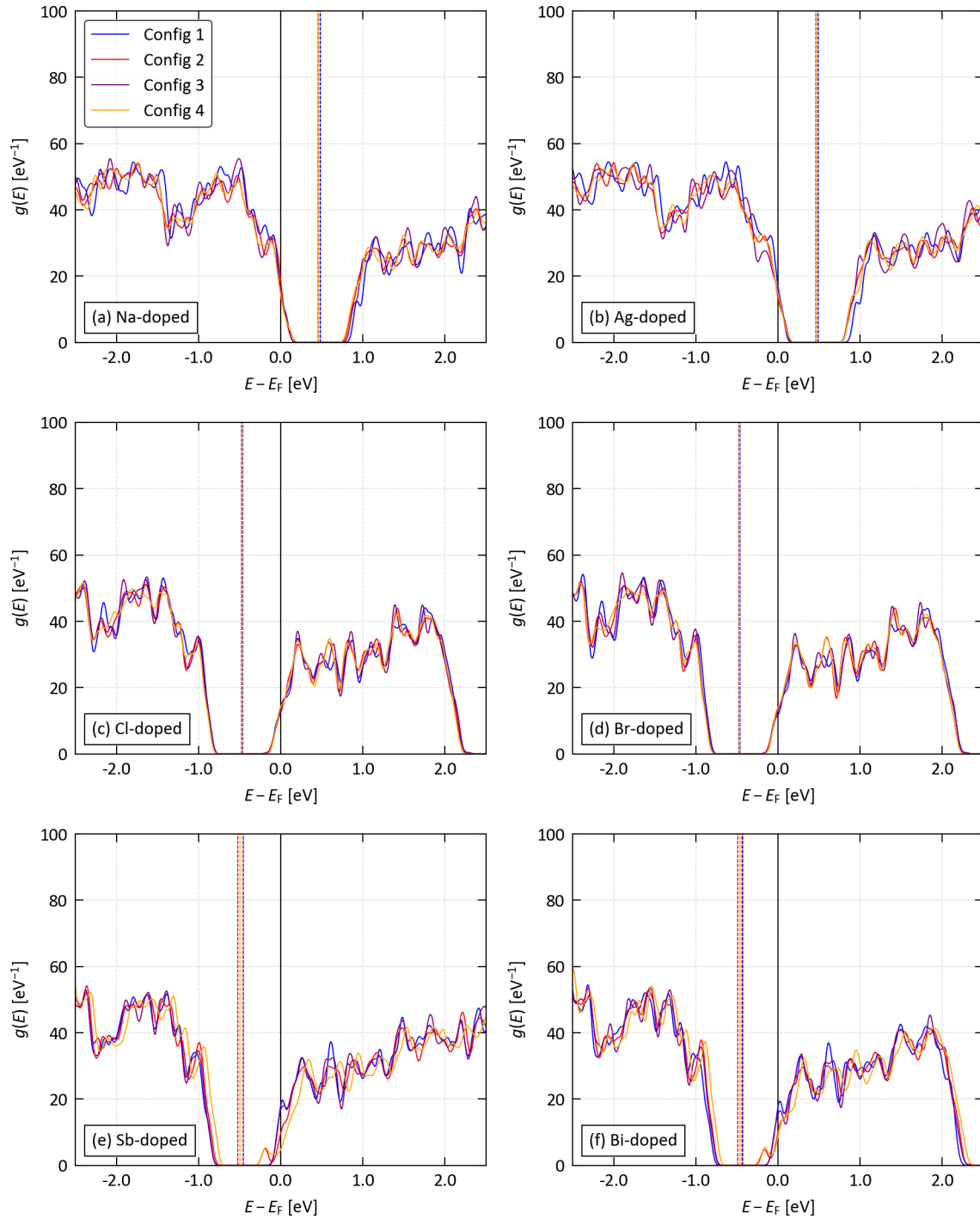


Fig. S24 Calculated electronic density of states (DoS) of π SnSe doped with Na (a), Ag (b), Cl (c), Br (d), Sb (e) and Bi (f). On each plot, the approximate midpoints of the host bandgaps, used to estimate the ionisation of the dopant atom, are shown as vertical dashed lines. These calculations were performed with the PBEsol functional and the bandgaps are underestimated compared to the more accurate non-self-consistent HSE06 calculations discussed in the text.

5 References

- 1 A. Togo, L. Chaput and I. Tanaka, *Physical Review B*, 2015, **91**, 094306.
- 2 J. Tang and J. M. Skelton, *Journal of Physics: Condensed Matter*, 2021, **33**, 164002.
- 3 J. M. Skelton, *Journal of Materials Chemistry C*, 2021, **9**, 11772–11787.
- 4 S. K. Guillemot, A. Suwardi, N. Kaltsoyannis and J. M. Skelton, *Journal of Materials Chemistry A*, 2024, **12**, 2932–2948.
- 5 G. K. Madsen, J. Carrete and M. J. Verstraete, *Computer Physics Communications*, 2018, **231**, 140–145.
- 6 A. M. Ganose, J. Park, A. Faghaninia, R. Woods-Robinson, K. A. Persson and A. Jain, *Nature Communications*, 2021, **12**, 2222.
- 7 Y. Liu, J. M. Skelton, X. Xia, Y. Zhu, D. J. Lewis and R. Freer, *Journal of Materials Chemistry C*, 2024, **12**, 508–520.
- 8 Z. M. Gibbs, F. Ricci, G. Li, H. Zhu, K. Persson, G. Ceder, G. Hautier, A. Jain and G. J. Snyder, *npj Computational Materials*, 2017, **3**, 8.
- 9 L.-D. Zhao, G. Tan, S. Hao, J. He, Y. Pei, H. Chi, H. Wang, S. Gong, H. Xu, V. P. Dravid *et al.*, *Science*, 2016, **351**, 141–144.
- 10 A. T. Duong, V. Q. Nguyen, G. Duvjir, V. T. Duong, S. Kwon, J. Y. Song, J. K. Lee, J. E. Lee, S. Park, T. Min, J. Lee, J. Kim and S. Cho, *Nature Communications*, 2016, **7**, 13713.
- 11 J. Dona, J. Archana, S. Kamalakannan, M. Prakash, K. Hara, S. Harish and M. Navaneethan, *Journal of Alloys and Compounds*, 2022, **899**, 163269.
- 12 Y. Iguchi, K. Inoue, T. Sugiyama and H. Yanagi, *Inorganic Chemistry*, 2018, **57**, 6769–6772.
- 13 X. Hu, W. He, D. Wang, B. Yuan, Z. Huang and L.-D. Zhao, *Scripta Materialia*, 2019, **170**, 99–105.
- 14 L. Su, T. Hong, D. Wang, S. Wang, B. Qin, M. Zhang, X. Gao, C. Chang and L.-D. Zhao, *Materials Today Physics*, 2021, **20**, 100452.
- 15 W. He, D. Wang, J.-F. Dong, Y. Qiu, L. Fu, Y. Feng, Y. Hao, G. Wang, J. Wang, C. Liu *et al.*, *Journal of Materials Chemistry A*, 2018, **6**, 10048–10056.
- 16 C. Yamamoto, X. He, T. Katase, K. Ide, Y. Goto, Y. Mizuguchi, A. Samizo, M. Minohara, S. Ueda, H. Hiramatsu, H. Hosono and T. Kamiya, *Advanced Functional Materials*, 2021, **31**, 2008092.
- 17 A. Jain, G. Hautier, S. P. Ong, C. J. Moore, C. C. Fischer, K. A. Persson and G. Ceder, *Physical Review B*, 2011, **84**, 045115.
- 18 A. Jain, S. P. Ong, G. Hautier, W. Chen, W. D. Richards, S. Dacek, S. Cholia, D. Gunter, D. Skinner, G. Ceder and K. A. Persson, *APL Materials*, 2013, **1**, 011002.
- 19 A. Glibo, M. Reda, Y. Surace, D. M. Cupid and H. Flandorfer, *Journal of Alloys and Compounds*, 2023, **969**, 172320.
- 20 R. Colin and J. Drowart, *Transactions of the Faraday Society*, 1964, **60**, 673–683.
- 21 G. Lindberg, A. Larsson, M. Råberg, D. Boström, R. Backman and A. Nordin, *The Journal of Chemical Thermodynamics*, 2007, **39**, 44–48.
- 22 T. L. Brundzia and O. J. Klep, *Economic Geology*, 1988, **83**, 174–181.
- 23 P. Scardala, V. Piacente and D. Ferro, *Journal of the Less Common Metals*, 1990, **162**, 11–21.
- 24 G. K. Johnson, G. Papatheodorou and C. E. Johnson, *The Journal of Chemical Thermodynamics*, 1981, **13**, 745–754.
- 25 V. R. Sidorko, L. V. Goncharuk and R. V. Antonenko, *Powder Metallurgy and Metal Ceramics*, 2008, **47**, 234–241.
- 26 I. Pallikara and J. M. Skelton, *Physical Chemistry Chemical Physics*, 2021, **23**, 19219–19236.
- 27 P. E. Blöchl, *Physical Review B*, 1994, **50**, 17953.
- 28 G. Kresse and D. Joubert, *Physical Review B*, 1999, **59**, 1758.

-
- 29 D. S. D. Gunn, J. M. Skelton, L. A. Burton, S. Metz and S. C. Parker, *Chemistry of Materials*, 2019, **31**, 3672–3685.
- 30 A. V. Krukau, O. A. Vydrov, A. F. Izmaylov and G. E. Scuseria, *The Journal of Chemical Physics*, 2006, **125**, 224106.
- 31 J. M. Skelton, D. S. Gunn, S. Metz and S. C. Parker, *Journal of Chemical Theory and Computation*, 2020, **16**, 3543–3557.
- 32 H. J. Monkhorst and J. D. Pack, *Physical Review B*, 1976, **13**, 5188.
- 33 E. R. Jette and F. Foote, *The Journal of Chemical Physics*, 1935, **3**, 605–616.
- 34 R. Jaggi, *Helvetica Physica Acta*, 1964, **37**, 618.
- 35 J. M. Skelton, L. A. Burton, A. J. Jackson, F. Oba, S. C. Parker and A. Walsh, *Physical Chemistry Chemical Physics*, 2017, **19**, 12452–12465.
- 36 T. Chattopadhyay, J. Pannetier and H. G. Von Schnering, *Journal of Physics and Chemistry of Solids*, 1986, **47**, 879–885.
- 37 J. M. Flitcroft, I. Pallikara and J. M. Skelton, *Solids*, 2022, **3**, 155–176.
- 38 M. Zhang, J. M. Flitcroft, S. K. Guillemot and J. M. Skelton, *Journal of Materials Chemistry C*, 2023, **11**, 14833–14847.